

1 Vertical structure of biomass burning aerosol transported over 2 the southeast Atlantic Ocean

3 Harshvardhan Harshvardhan¹, Richard Ferrare², Sharon Burton², Johnathan Hair², Chris
4 Hostetler², David Harper², Anthony Cook², Marta Fenn³, Amy Jo Scarino³, Eduard Chemyakin³,
5 Detlef Müller⁴

6 ¹Purdue University, West Lafayette, IN, United States

7 ²NASA Langley Research Center, Hampton, VA, United States

8 ³Science Systems and Applications, Inc./NASA Langley Research Center, Hampton, VA, United States

9 ⁴University of Hertfordshire, Hatfield, Hertfordshire, United Kingdom

10 *Correspondence to:* H. Harshvardhan (harshvar@purdue.edu)

11 **Abstract.** Biomass burning in southwestern Africa produces smoke plumes that are transported over the Atlantic
12 Ocean and overlie vast regions of stratocumulus clouds. This aerosol layer contributes to direct and indirect radiative
13 forcing of the atmosphere in this region, particularly during the months of August, September and October. There was
14 a multi-year international campaign to study this aerosol and its interactions with clouds. Here we report on the
15 evolution of aerosol distributions and properties as measured by the airborne high spectral resolution lidar (HSRL-2)
16 during the ORACLES (Observations of Aerosols above Clouds and their intEractionS) campaign in September 2016.
17 The NASA Langley HSRL-2 instrument was flown on the NASA ER-2 aircraft for several days in September 2016.
18 Data were aggregated at two pairs of 2°×2° grid boxes to examine the evolution of the vertical profile of aerosol
19 properties during transport over the ocean. Results showed that the structure of the profile of aerosol extinction and
20 microphysical properties is maintained over a one to two-day time scale. In the 3-5 km altitude range, 95% of the
21 aerosol extinction was contributed by particles in the 0.05-0.50 μm radius size range, with the aerosol in this size
22 range having an average effective radius of 0.16 μm. This indicates that there is essentially no scavenging or dry
23 deposition at these altitudes. Moreover, there is very little day to day variation in these properties, such that time
24 sampling as happens in such campaigns, may be representative of longer periods such as monthly means. Below 3 km
25 there is considerable mixing with larger aerosol, most likely continental source near land. Furthermore, these
26 measurements indicated that there was often a distinct gap between the bottom of the aerosol layer and cloud tops at
27 the selected locations as evidenced by a layer of several hundred meters that contained relatively low aerosol extinction
28 values above the clouds.

29 1 Introduction

30 Aerosols are often considered as the most confounding element in the climate system when simulating parameters of
31 the Earth's current climate. Their interaction with clouds makes the problem extremely complicated. The general topic
32 of aerosol-cloud interaction has been of great interest in the scientific community: to quote the report of the
33 Intergovernmental Panel on Climate Change (IPCC AR5) "Clouds and aerosols continue to contribute the largest
34 uncertainty to estimates and interpretations of the Earth's changing energy budget" (Boucher et al., 2013).

Deleted: The fraction of aerosol in the fine mode between 50 and 500 nm remained above 0.95 and the effective radius of this fine mode was 0.16 μm from 3 to 5 km in altitude.

Deleted: future

Deleted: c

Deleted: limate

41 In the context of these interactions, the interplay of biomass burning (BB) aerosol and the stratocumulus clouds in
42 the South East (SE) Atlantic is unique and crucial to the estimates of the energy budget of the region. This BB aerosol
43 arises from the seasonal burning (July-October) of agricultural residue in the southwestern African Savannah and
44 traverses large distances westward over the SE Atlantic Ocean. Unlike the aerosol from industrial activity and biofuels
45 that intermingle with clouds in many regions (Ramanathan et al., 2001; Mechoso et al., 2013), these optically thick
46 BB aerosol layers overlay vast stretches of marine stratus cloud in the SE Atlantic (Chand et al., 2009; Wilcox, 2010;
47 Adebisi et al., 2015) where they have a direct radiative effect. The BB aerosol can also act as nuclei for cloud droplets
48 and so cause a potentially significant cloud albedo effect. Observations and modelling studies of such interactions in
49 the Southeast Atlantic and southern Africa regions are in Diamond et al. (2018), Kacarab et al. (2020) and Gupta et
50 al. (2021). There is also some evidence that aerosol can alter the thermodynamics of cloud formation through semi-
51 direct effects (Sakaeda et al., 2011). Studies using high resolution limited area models have shown a variety of effects,
52 including stratus to cumulus transition resulting from these interactions (Yamaguchi et al., 2015; Gordon et al., 2018;
53 Lu et al., 2018). The semi-direct effect has also been shown to be important in a limited time run of a global model
54 (Das et al., 2020).

Deleted: South East

55 During the course of its transport over the Atlantic basin, the dense BB aerosol layer affects the underlying clouds
56 and Earth's radiative balance in multiple ways. It exerts a direct radiative forcing (DRF) on the atmosphere by
57 absorbing the incoming solar radiation along with the radiation reflected by the underlying cloud surface (Chand et
58 al., 2009; Meyer et al., 2013; Zhang et al., 2016). Simultaneously, depending on the relative vertical location of the
59 aerosol with respect to the cloud deck, the cloud cover (fraction) or liquid water path may increase or decrease in
60 response to heating of surrounding air masses due to aerosol absorption and subsequent changes in atmospheric
61 stability, the semi-direct forcing (Sakaeda et al., 2011; Wilcox, 2012; Das et al., 2020). Moreover, as the marine
62 boundary layer (MBL) deepens farther offshore and north of 5° S, subsiding aerosol particles become entrained into
63 the MBL and interact with the clouds as cloud condensation nuclei to affect their microphysics (indirect forcing)
64 (Costantino and Breon, 2013; Painemal et al., 2014).

Deleted: mostly

65 In the context of simulating the above alluded aerosol radiative effects, it is vital that aerosol-cloud overlap
66 characteristics are accurately represented within the models. The quantification of these aerosol-cloud overlap
67 characteristics in the models is necessary for a variety of reasons. For example, previous studies have found that the
68 sign and magnitude of DRF of absorbing aerosol above clouds (AAC) critically depends upon the reflectance and
69 coverage of the underlying cloud surfaces along with the optical properties, composition and size distribution of the
70 overlying aerosols (Keil and Haywood, 2003; Chand et al., 2009). Additionally, the magnitude and sign of the aerosol
71 semi-direct effects are quite sensitive to the vertical distribution of aerosols, especially with respect to the vertical
72 location of clouds (Penner et al., 2003; McFarquhar and Wang, 2006; Koch and Del Genio, 2010).

73 Here we address the evolution of the vertical properties of BB aerosol as it travels in the marine environment after
74 leaving the African land mass. Section 2 identifies the field campaign and specifies the geographic region selected for
75 the analysis and rationale for that choice. Section 3 describes the attributes of the instrument and key parameters
76 related to the aerosol that can be extracted from the measurements. Section 4 presents the results followed by a
77 summary and conclusion in section 5.

80 **2 Field Campaigns**

81 The concerns mentioned above were the driving force behind plans for several international multi-year field
82 campaigns; ORACLES (Observations of Aerosols above Clouds and their intEractionS, Redemann et al., 2021),
83 CLARIFY-2017 (CLoud-Aerosol-Radiation Interactions and Forcing for Year 2017, [Haywood et al., 2021](#)), and
84 LASIC (Layered Atlantic Smoke Interactions with Clouds, Zuidema et al., 2016, 2018). A key component of the
85 September 2016 NASA ORACLES Intensive Observation Period (IOP) was the vertical profiling of aerosol properties
86 measured by an airborne lidar, the NASA Langley High Spectral Resolution Lidar-2, HSRL-2 (Burton et al., 2018),
87 on-board the NASA ER-2, which was based in Walvis Bay, Namibia, for operations during 2016. In the following
88 two years, the instrument was on-board the P-3 flying out of São Tomé. The siting and flight tracks chosen ensured
89 adequate coverage of the seasonal BB aerosol.

90 **2.1 Meteorology**

91 The monthly mean meteorological situation is shown in Fig. 1 from MERRA2 reanalysis (Buchard et al., 2017;
92 Randles et al., 2017) along with locations of relevant sites. A thorough meteorological analysis for all ORACLES
93 IOPs is provided in Ryoo et al. (2021). For the period under consideration here, they found that the African Easterly
94 Jet-South (AEJ-S) was active and corresponded closely to the long-term climatology. Fig. 2 shows 650 hPa winds
95 from MERRA2 reanalysis at the beginning, at the end, and on two intermediate days during which HSRL-2
96 measurements were made. ER-2 flight tracks during the September 2016 IOP are shown in Fig. 3. Note that flights
97 were primarily confined to within roughly 1000 km of the African coast with only the 22 September flight venturing
98 further. Flights such as executed during the IOP are unable to follow air parcels in a Lagrangian fashion to examine
99 the evolution of smoke plumes. Here we provide an alternate framework by which to study evolving aerosol properties
100 in an average sense. In order to establish average characteristics of the BB smoke plume as it travels over the ocean,
101 we have chosen five grid boxes of two-degree latitude and longitude on a side at various distances from the source
102 and aggregated observations. The choice of grid boxes was based on the availability of data from the flights (Fig. 3)
103 and the general direction of transport of the smoke as evidenced by the wind fields in Fig. 2. The grid boxes so chosen
104 are marked on Figs. 2 and 3 and the rationale for the choice is explained below.

105 Figure 4 shows 48-hour backward trajectory frequency analyses at 3.5 km, roughly the central altitude of the plume,
106 using NOAA HYSPLIT trajectory calculations (https://www.ready.noaa.gov/HYSPLIT_traj.php) which were carried
107 out using archived GDAS 0.5-degree meteorology (Stein et al., 2015). The frequency distribution is a 48-hour history
108 of the paths taken by air parcels arriving at the grid boxes marked A and C at 3500 m altitude. The time period of the
109 frequency analyses covers the entire period during which HSRL-2 measurements were made, 12-24 September 2016.
110 The selected grid box pairs indicate that Box A receives aerosol that has earlier crossed Box B and Box C is downwind
111 of Box D; boxes B and D receive aerosol directly from BB sources on land. The grid box pairs A/B and C/D can
112 therefore provide information on the evolution of the microphysics and vertical distribution of BB aerosol plumes

Deleted: ¶

Deleted: Wu

Deleted: 0

Formatted: Font: Bold, Complex Script Font: Bold

Formatted: Indent: First line: 0.13"

Deleted: overall

Deleted: 2

Deleted: based on backward trajectory analyses.

Deleted: 3

Deleted: center of

123 after leaving the continent. This strategy is similar to that used in comparisons of models with observations for this
124 campaign by Shinozuka et al. (2020), who also showed that observations made on the sampled days were
125 representative of monthly means. In addition to the four boxes strongly influenced by smoke, a southern box, E, has
126 been chosen to provide a control contrast to the other areas in that it is influenced primarily by maritime air as seen
127 from Figs. 1 and 2.

Deleted: The location of the five grid boxes is also shown superimposed on flight tracks in Fig. 2.

128 **2.2 ORACLES 2016 IOP**

129 The days during the campaign that were included in the averaging procedure are shown in Table 1. Also included
130 is the typical time of the day when the measurements were made, a function of the flight pattern of the ER-2. The
131 number of lidar return profiles averaged for each grid box and statistics related to the backward trajectories are also
132 listed. These grid boxes contained aircraft tracks on multiple days during which trajectory analysis showed near-
133 uniform wind direction between 2.5 and 4.5 km altitude throughout the IOP. With the exception of the grid box
134 centered at 22° S, 9° E, all indicate flow from the source region of BB aerosol. Table 1 also lists the mean and standard
135 deviation of time duration in hours spent over water of air parcels arriving at 3500 m altitude at the grid box during
136 the averaging period. There is no entry for Box E since arriving air had a maritime source and did not originate from
137 land. It must be stressed that the duration is not calculated from the source region on land, which is distributed over a
138 large area of central Africa (e.g., Fig. 9 of Redemann et al., 2021) and cannot be uniquely identified with specific
139 observations made over the ocean. The plume has already been airborne over land for several hours (see Fig. 4) and
140 aerosol would have undergone transformations that occur at short time scales (Cappa et al., 2020). The duration was
141 calculated by running HYSPLIT backward trajectories of air parcels arriving every six hours starting at 0600 UTC on
142 the days of the first flight and ending at 1800 UTC on the days of the last flight of the averaging period and is shown
143 in some detail in Fig. 5, which essentially reflects the profile of the prevailing wind speeds. The inference is that BB
144 smoke at 3500 m altitude arrives at A on average about 30 h after passing B and arrives at C 35 h after passing D. The
145 change in selected aerosol properties as measured by the HSRL-2 during this travel in the marine environment provides
146 information on the evolution of the plume during this time period.

Deleted: ¶

Deleted: center

Deleted: 3

Deleted: 4

147 **3 HSRL-2**

148 The NASA LaRC HSRL-2 uses the HSRL technique to independently retrieve aerosol extinction and backscatter
149 (Shiple et al., 1983; Grund and Eloranta, 1991; She et al., 1992) without a priori assumptions on aerosol type or
150 extinction-to-backscatter ratio. By using the HSRL technique, HSRL-2, like its predecessor HSRL-1 (Hair et al.,
151 2008), provides accurate backscatter profiles even in situations where the lidar beam is attenuated by overlying cloud
152 or aerosol as long as it is not completely attenuated. The LaRC HSRL-2 employs the HSRL technique at 355 and 532
153 nm and the standard backscatter technique at 1064 nm. It also measures aerosol and cloud depolarization at all three
154 wavelengths. The HSRL-2 provides vertically resolved measurements of the following extensive and intensive aerosol

Deleted: and tenuous cloud

Deleted:

163 parameters below the aircraft (approximate archival horizontal, Δx , and vertical resolutions, Δz , are listed assuming
164 ER-2 cruise speed).

165 • *Extensive parameters*¹ – backscatter coefficient, β , at 355, 532 and 1064 nm ($\Delta x \sim 2$ km, $\Delta z \sim 15$ m); extinction
166 coefficient, α , at 355, and 532 nm ($\Delta x \sim 12$ km, $\Delta z \sim 300$ m); optical depth at 355 and 532 nm (integrating the profile
167 of extinction). The aerosol optical depth (AOD) is a critical quantity in discussions of the influence of aerosol on
168 climate (Boucher et al., 2013).

169 • *Intensive parameters* – extinction-to-backscatter ratio of aerosol, the Lidar Ratio, $S_a = \alpha_a / \beta_a$, at 355 and 532 nm
170 ($\Delta x \sim 12$ km, $\Delta z \sim 300$ m); depolarization, $\delta_a = \beta_a^\perp / \beta_a^\parallel$, at 355, 532, and 1064 nm ($\Delta x \sim 2$ km, $\Delta z \sim 15$ m); and
171 aerosol backscatter wavelength dependence (i.e., Ångström exponent for aerosol backscatter – directly related to the
172 backscatter color ratio) for two wavelength pairs (355-532 and 532-1064 nm, $\Delta x \sim 2$ km, $\Delta z \sim 15$ m).

173 The overall systematic error associated with the backscatter calibration is estimated to be less than 5 % for the 355
174 and 532 nm channels and 20 % for 1064 nm (Burton et al., 2015). Under typical conditions, the total systematic error
175 for extinction is estimated to be less than 0.01 km⁻¹ at 532 nm. The random errors for all aerosol products are typically
176 less than 10 % for the backscatter and depolarization ratios (Hair et al., 2008). Rogers et al. (2009) validated the HSRL
177 extinction coefficient profiles and found that the HSRL extinction profiles are within the typical state-of-the-art
178 systematic error at visible wavelengths (Schmid et al., 2006). Since HSRL-2 includes the capability to measure
179 backscatter at three wavelengths and extinction at two wavelengths, “3 β +2 α ” microphysical retrieval algorithms
180 (Müller et al., 1999a, 1999b; Veselovskii et al., 2002) are used to retrieve height-resolved parameters such as aerosol
181 effective radius and number, surface and volume concentrations (Müller et al., 2014, Sawamura et al., 2016). [Here we](#)
182 [restrict ourselves to the effective radius of the particles.](#)

183 4 Results

184 In this study of the vertically resolved evolving properties of BB aerosol, we present key lidar measurements and
185 microphysical results obtained by performing the “3 β +2 α ” retrieval mentioned in Section 3.

186 4.1 Lidar

187 Vertical profiles averaged over the times of overflight in 2°×2° latitude/longitude boxes shown in Figure 3 on the
188 days given in Table 1 are for the following properties.

¹ By the term *extensive*, we refer to optical parameters, such as extinction, that are influenced by the amount (concentration) and type (size, composition, shape) of aerosol/cloud particles. *Intensive* properties, on the other hand, are those that depend only on the nature of the particles and not on their quantity or concentration, but rather depend only on aerosol type (Anderson et al., 2003).

Formatted: Indent: First line: 0.13", Space After: 0 pt

Deleted: ,

- 190 1. Aerosol Extinction at 532 nm, α_a , ~~determined by aerosol number concentration, microphysical~~
- 191 ~~properties and relative humidity,~~
- 192 2. Backscatter Ångström exponent between 1064 and 532 nm, an indication of particle size.
- 193 3. Aerosol Depolarization at 532 nm, a measure of particle asphericity.
- 194 4. Aerosol extinction to backscatter ratio, the Lidar Ratio, at 532 nm, a marker for aerosol composition.

Deleted: the primary measure of aerosol abundance

Deleted: .

195 Inspection of the wind field at 650 hPa in Fig. 2 and backward trajectory frequency plots in Fig. 4 suggest that the

196 grid boxes chosen fit naturally into two pairs of tracks of the widespread BB aerosol field. The northern pair, identified

197 in Table 1 as A and B, centered around 10° S, are in a faster zonal track, whereas the grid boxes C and D are in a track

198 centered between 13-15° S that is slightly slower and has a component from the north over a stretch of water (Fig. 2).

199 The two pairs can then provide information on the evolution of aerosol properties over a time scale of one to two days.

200 Figures 6-9 show the aerosol extinction, backscatter Ångström exponent, aerosol depolarization and Lidar Ratio for

201 the two pairs of grid boxes and Box E, which is not significantly influenced by the BB aerosol. The results presented

202 are one-minute averages of independent 10 s vertical profiles for backscatter Ångström exponent and depolarization

203 and one-minute averages for extinction and lidar ratio profiles. From Table 1, the mean time elapsed between B and

204 A is 29.4 h and that between D and C is 34.9 h. It should be pointed out that parameter values shown below the level

205 of mean cloud top are averages of lidar returns through breaks in the stratus deck and are not relevant for this study.

206 If we use the low cut-off of an extinction coefficient of 15 Mm⁻¹ to indicate an aerosol-free layer (Shinozuka et al.,

207 2020), then Fig. 6 indicates that the bulk of the smoke layers encountered at these distances from land were separated

208 from the cloud top, a feature more prevalent during the 2016 IOP than in 2017 and 2018 (Redemann et al., 2021).

Deleted: 1

Deleted: 3

Formatted: Indent: First line: 0.13", Space After: 0 pt

Deleted: and Fig. 3

209 The northern plume is a column of aerosol of relatively constant extinction from just above 2.5 km to 5 km while

210 the southern plume has a profile of extinction that increases nearly linearly with height from a minimum near the cloud

211 top to a maximum at 5 km (Fig. 6). The vertical structure of the aerosol profiles measured by HSRL-2 was compared

212 to water vapor profiles represented by the Modern-Era Retrospective analysis for Research and Applications, Version

213 2 (MERRA2) model. Pistone et al. (2021) explored the relationship between aerosols, CO, water vapor as measured

214 by ORACLES airborne in situ measurements and represented by models including MERRA2. They found the

215 MERRA2 water vapor profiles, like the measured water vapor profiles, exhibited a linear relationship with CO and

216 biomass burning plume strength; they also found that smoky, humid air produced by daytime convection over the

217 continent advected over the ocean and into the ORACLES study region. MERRA2 water vapor profiles produced at

218 three hourly increments and 72 pressure levels were interpolated to the times and locations of the HSRL-2 profiles.

219 Water vapor mixing ratio generally decreased significantly just above the PBL then increased for altitudes around 2

220 to 3 km before decreasing again. This behavior is generally consistent with the relationship between water vapor and

221 aerosol scattering reported by Pistone et al. (2021).

Deleted: essentially

Formatted: Font: 10 pt, Complex Script Font: 10 pt

Formatted: Font: 10 pt, Complex Script Font: 10 pt

222 Figure 10 shows the median, 25th and 75th percentile relative humidity (RH) profiles computed by interpolating the

223 MERRA2 0.5-deg. 3-hourly humidity profiles to the locations and times of the HSRL-2 measurements. The profiles

224 typically show a more pronounced increase in RH with altitude that more closely follows the HSRL-2 measurements

225 of aerosol extinction profiles, although the MERRA2 profiles typically begin decreasing above 4 km whereas the

226 airborne in situ RH measurements and HSRL-2 aerosol extinction profiles begin decreasing above 5 km. Interestingly,

Formatted: Font: 10 pt, Complex Script Font: 10 pt

Formatted: Font: 10 pt, Complex Script Font: 10 pt

Formatted: Superscript

Formatted: Superscript

Formatted: Font: 10 pt, Complex Script Font: 10 pt

Formatted: Font: 10 pt, Complex Script Font: 10 pt

Formatted: Font: 10 pt, Complex Script Font: 10 pt

Formatted: Font: 10 pt, Complex Script Font: 10 pt

Formatted: Font: 10 pt, Complex Script Font: 10 pt

235 during three of the dates (Sept. 12, 16, 22) considerable portions of the smoke layers correspond to MERRA2 relative
236 humidity above 60-70%. This increase in RH with altitude could help explain at least some of the increase in aerosol
237 extinction with height observed in the HSRL-2 profiles of the C/D Box pair. Aerosol humidification often amplified
238 the increase in aerosol extinction by factors of 1.5 or more (Doherty et al., 2022).

- Formatted: Font: 10 pt, Complex Script Font: 10 pt
- Formatted: Font: 10 pt, Complex Script Font: 10 pt
- Formatted: Font: 10 pt, Complex Script Font: 10 pt
- Formatted: Font: 10 pt, Complex Script Font: 10 pt

239 The Ångström exponent (Fig. 7) and depolarization (Fig. 8) indicate the presence of fine spherical particles at the
240 top of the plume and increasing sizes towards the bottom. The Lidar Ratio (Fig. 9) above 3 km for the two pairs is
241 between 70 and 80 sr, suggesting strong absorption (Müller et al., 2019) but is considerably less and highly variable
242 in Box E and in the lower layers of the aerosol plume in Box D, where the smoke plume most likely has components
243 of continental aerosol such as dust and pollution typical of the nearby Namibian coast (Klopper et al., 2020). The most
244 striking feature of the results is the very small profile-to-profile variability of the intensive lidar parameters in the
245 upper two kilometers of the plume over the course of several days as evident from the range of values in the 25-75
246 percentile shaded grey in Figs. 7-9. This suggests strongly that the particles maintain their size, shape and absorbing
247 properties over the first few days of transport over the ocean. This result is of some importance for climate studies in
248 which the radiative properties of BB aerosol are input to the calculation of radiative forcing. Complex chain aggregates
249 as found near the source of fires (Pósfai et al., 2003, China et al., 2013) are typically not represented in climate models.
250 However, if the aerosol is already spherical and maintains its size over the time period of radiative interactions being
251 studied, then core-shell models of varying degrees of complexity could perhaps suffice (Zhang et al., 2020). The lower
252 portion of the plume containing larger BB aerosol particles is subject to mixing with marine and continental particles
253 from regions not affected by biomass burning and is highly variable in nature. This would be more difficult to model
254 but Fig. 6 shows that the aerosol extinction coefficient decreases rapidly at lower levels so errors in representation
255 may be acceptable.

- Deleted: has components of continental
- Deleted:
- Deleted: are the near constant values
- Deleted: these
- Deleted: 6 and
- Deleted: 7
- Deleted: original particles near the source of combustion have been coated before they cross the land-ocean boundary and ...
- Deleted: The lower portion of the plume containing larger BB aerosol particles is subject to mixing with other particles and is highly variable in nature.
- Deleted: coated

256 **4.2 Microphysics**

257 The lidar measurements are inverted to obtain information regarding particle size. The inversion is performed on one-
258 minute averages of six independent 10 s backscatter profiles and one-minute average extinction profiles. Details of
259 the inversion process are in Müller et al. (2019) and references therein. The particle size distribution is represented
260 using a series of eight triangular basis functions that can represent both monomodal and bimodal size distributions
261 (*ibid*). Points to note are that the procedure makes the following assumptions: the particles are spherical and
262 homogeneous having wavelength-independent complex index of refraction. The low (< 5 %) values of depolarization
263 through most of the plume, shown in Fig. 8, suggests that the spherical assumption is justified. There is most likely
264 structure and inhomogeneity in the core of the particles, but current particle optical models are unable to incorporate
265 these complexities. Results from this inversion procedure have been compared to coincident airborne in situ particle
266 measurements. Müller et al. (2014) present results from a campaign off the northeast coast of the US showing that the
267 inversion results agree with in situ measurements of effective radius and also number, surface area and volume
268 concentration within error bars. Sawamura et al. (2017) report on campaigns in the wintertime San Joaquin Valley of
269 California and summertime near Houston, TX. They found high correlation and low bias in surface and volume

- Deleted: 7

284 concentration in situ measurements relative to HSRL with the best agreement for submicron fine-mode aerosol, which
285 is most relevant to the current study. Müller et al. (2019) report retrievals and their uncertainty for one day in the
286 ORACLES campaign, 22 September 2016. Considering only optical data with strong signal-to-noise ratio, they
287 estimate retrieval errors are 25 % for number concentration. The relative uncertainty in effective radius for parts of
288 the flight track where particle size was nearly constant was below 20 %.

289 In order to help separate particles that have BB source from coarser particles of continental or marine origin, we
290 specify a Submicron Fraction (SMF) as the contribution to the extinction at 532 nm of particles in the radius range
291 0.05-0.50 μm (Anderson et al., 2005). Figure 11 shows the profiles of SMF for the five grid boxes and not surprisingly,
292 the bulk of the smoke plume, especially between 3 and 5 km contains aerosol almost entirely in the submicron range.
293 Below 3 km, at locations both near and further way from the coast, there is a marked increase in the fraction of larger
294 particles. The increase in depolarization (Fig. 8) at these lower levels and a decrease in the Lidar Ratio (Fig. 9) suggest
295 mixing with the aforementioned non-BB aerosol particles. However, the sharp decrease in extinction below 3 km (Fig.
296 6) indicates that their contribution to direct radiative effects would be minimal. Finally, Fig. 12 shows the vertical
297 profile of the effective radius of the SMF aerosol population. The effective radius is 0.16 μm with little variation
298 between 3 and 5 km. Of greater significance is that it remains very similar between the pairs of grid boxes along the
299 transport trajectory of the smoke. The retrieved effective radius is similar to the results presented by Müller et al.
300 (2014) for a mixture of urban aerosol and smoke. Their comparison with in situ measurements showed a slight
301 overestimate but within a standard deviation. The retrieved and in situ results also show that the particle size is uniform
302 with altitude even when the number concentration drops by a factor of three. Another set of prior comparisons of
303 HSRL-2 and in situ measurements is provided in Sawamura et al. (2017). Here again, the effective radius of the
304 submicron fraction of particles, 0.15 μm , is uniform with altitude, and comparable though biased slightly low
305 compared to in situ observations.

306 5 Conclusions

307 The results of the aggregated HSRL-2 profiles during the 2016 ORACLES IOP presented here show two main
308 findings. These are however limited to a brief period in the transport of BB smoke from continental Africa over marine
309 clouds in the Atlantic Ocean. This is a limitation of the 2016 campaign because the flight tracks remained within 1000
310 km of the coast. For the period of one to two days after crossing the land-ocean boundary, the fraction of all particles
311 that are in the submicron range in the main smoke plume between 3 and 5 km is around 95 %. The effective radius of
312 the submicron particles in this altitude interval is 0.16 μm and essentially constant with altitude. The particle size is
313 comparable to measured particle sizes in previous campaigns that sampled aerosol that was a mixture of urban haze
314 and smoke (Müller et al., 2014; Sawamura et al., 2017). Moreover, the shape of the median vertical profile of
315 extinction does not change during the first two days of transport over water suggesting the absence of dry deposition
316 and wet scavenging. The low (< 0.05) depolarization ratio of the submicron particles signifies that they are well coated
317 and the assumption of sphericity in the inversion procedure and models that estimate the radiative effects of aerosol
318 is justified. The BB aerosol mix with continental and marine aerosol at the base of the plume but during the September

Deleted: 50
Deleted: nm-500 nm
Deleted: 9
Deleted: -
Deleted: 7
Deleted: 8
Deleted: continental and marine
Deleted: 5
Deleted: 0
Deleted: ± 0.1
Deleted: throughout the vertical extent of the plume

Deleted: range
Deleted: 0.15-

Deleted: y

333 2016 IOP this layer of mixed aerosol tended to ~~have very low extinction coefficients suggesting low abundance~~ and
334 there was ~~often~~ a distinct gap between the plume and the cloud tops.

335 The HSRL-2 instrument was also deployed in the 2017 and 2018 ORACLES campaigns but was ~~deployed on the~~
336 ~~NASA~~ P-3 which often flew at low altitude to acquire in situ measurements of aerosols and clouds. Consequently, the
337 HSRL_2 was not able to make continuous measurements of the BB aerosol plumes in a manner similar as when
338 deployed on the ER-2. However, there are segments of the track that can provide ~~similar~~ information ~~to the data~~
339 obtained in the 2016 campaign but for a different time period. Moreover, some flight tracks extended much further
340 from land (Doherty et al., 2021). Analysis of the later campaigns will provide information on the physical evolution
341 of aerosol that has aged for a longer period than is covered in this study.

Deleted: be very tenuous

Deleted: mounted

Deleted: a

Deleted: similar

Deleted: those

342 Data Management

343 HSRL-2 optical data and retrieved inversion data are available at the NASA archive site
344 <https://espoarchive.nasa.gov/archive/browse/oracles/id8/ER2> and are permanently archived at
345 doi:10.5067/SUBORBITAL/ORACLES/ER2/2016_V1.

346 Acknowledgements

347 The lead author would like to thank NASA Langley Research Center for hosting him during a sabbatical when this
348 study was initiated. HSRL-2 participation in ORACLES was supported by NASA through the Earth Venture
349 Suborbital-2 (EVS-2) program (grant no. 13-EVS2-13-0028). Funding for this work was also provided by NASA
350 through the Radiation Sciences Program. We wish to thank the NASA ER-2 pilots and ground crew for their extensive
351 support during ORACLES.

352

358 **References**

359 Anderson, T. L., Charlson, R. J., Winker, D. M., Ogren, J. A., and Holmén, K.: Mesoscale variations of tropospheric
360 aerosols, *J. Atmos. Sci.*, 60(1), 119-136, 2003.

361 Anderson, T. L., Wu, Y., Chu, D. A., Schmid, B., Redemann, J., and Dubovik, O.: Testing the MODIS satellite
362 retrieval of aerosol fine-mode fraction, *J. Geophys. Res.*, 110, D18204, doi:10.1029/2005JD005978, 2005.

363 Adebiyi, A. A., Zuidema, P., Chang, I., Burton, S. P., and Cairns, B.: Mid-level clouds are frequent above the Southeast
364 Atlantic stratocumulus clouds, *Atmos. Chem. Phys.*, 20, 11025-11043, doi:10.5194/acp-20-11025-2020, 2020.

365 Boucher, O., Randall, D., Artaxo, P., Bretherton, C., Feingold, G., Forster, P., Kerminen, V.-M. Kondo, Y., Liao, H.,
366 Lohmann, U., Rasch, P., Satheesh, S. K., Sherwood, S., Stevens, B., and Zhang X.Y.: Clouds and Aerosols. In:
367 Climate Change 2013: The Physical Science Basis. Contribution of Working Group I to the Fifth Assessment Report
368 of the Intergovernmental Panel on Climate Change [Stocker, T. F., Qin, D., Plattner, G.-K., Tignor, M., Allen, S.
369 K., Boschung, J., Nauels, A., Xia, Y., Bex V., and Midgley, P. M. (eds.)]. Cambridge University Press, 2013.

370 Buchard, V., Randles, C. A., da Silva, A. M., Darnenov, A., Colarco, P. R., Govindaraju, R., Ferrare, R. A., Hair, J.,
371 Beyersdorf, A. J. Ziemba L. D., and Yu, H.: The MERRA-2 aerosol reanalysis, 1980 onwards Part II: Evaluation
372 and case studies, *J. Climate*, 30, 6851-6871, doi:10.1175/JCLI-D-16-0613.1, 2017.

373 Burton, S. P., Hostetler, C. A., Cook, A. L., Hair, J. W., Seaman, S., Scola, S., Harper, D. B., Smith, J. A., Fenn, M
374 A., Ferrare, R. A., Saide, P. E., Chemyakin, E. V., and Müller, D.: Calibration of a high spectral resolution lidar
375 using a Michelson interferometer with data examples from ORACLES, *Appl. Optics*, 57, 6061-6075, 2018.

376 Burton, S. P., Hair, J. W., Kahnert, M., Ferrare, R. A., Hostetler, C. A., Cook, A. L., Harper, D. B., Berkoff, T. A.,
377 Seaman, S. T., Collins, J. E., Fenn, M. A., and Rogers, R. R.: Observations of the spectral dependence of linear
378 particle depolarization ratio of aerosols using NASA Langley airborne High Spectral Resolution Lidar, *Atmos.*
379 *Chem. Phys.*, 15, 13453–13473, doi.org/10.5194/acp-15-13453-2015, 2015.

380 Cappa, C. D., Lim, C. Y., Hagan, D. H., Coggon, M., Koss, A., Sekimoto, K., de Gouw, J., Onasch, T. B., Warneke,
381 C., and Kroll, J. H.: Biomass-burning-derived particles from a wide variety of fuels – Part 2: Effects of
382 photochemical aging on particle optical and chemical properties, *Atmos. Chem. Phys.*, 20, 8511-8532,
383 doi:10.5194/acp-20-8511-2020, 2020.

384 Chand, D., Wood, R., Anderson, T. L., Satheesh, S. K., and Charlson, R. J.: Satellite-derived direct radiative effect of
385 aerosols dependent on cloud cover, *Nat. Geosci.*, 2, 181-184, doi:10.1038/Ngeo437, 2009.

386 China, S., Mazzoleni, C., Gorkowski, K., Aiken, A. C., and Dubey, M. K.: Morphology and mixing state of individual
387 freshly emitted wildfire carbonaceous particles, *Nat. Commun.*, 4:2122 doi: 10.1038/ncomms3122, 2013.

388 Costantino, L., and Bréon F. M.: Aerosol indirect effect on warm clouds over South-East Atlantic from co-located
389 MODIS and CALIPSO observations, *Atmos. Chem. Phys.*, 13, 69-88, doi:10.5194/acp-13-69-2013, 2013.

390 Das, S., Harshvardhan, H., and Colarco, P. R.: The influence of elevated smoke layers on stratocumulus clouds over
391 the SE Atlantic in the NASA Goddard Earth Observing System (GEOS) Model, *J. Geophys. Res. Atmos.*, 125,
392 e2019JD031209. doi:10.1029/2019JD031209, 2020.

393 Diamond, M. S., Dobracki, A., Freitag, S., Small Griswold, J. D., Heikkilä, A., Howell, S. G., Kacarab, M. E.,
394 Podolske, J. R., Saide, P. E., and Wood, R.: Time-dependent entrainment of smoke presents an observational
395 challenge for assessing aerosol–cloud interactions over the southeast Atlantic Ocean, *Atmos. Chem. Phys.*, 18,
396 14623–14636, <https://doi.org/10.5194/acp-18-14623-2018>, 2018.

397 Doherty, S. J., Saide, P. E., Zuidema, P., Shinozuka, Y., Ferrada, G. A., Gordon, H., Mallet, M., Meyer, K.,
398 Painemal, D., Howell, S. G., Freitag, S., Dobracki, A., Podolske, J. R., Burton, S. P., Ferrare, R. A., Howes, C.,
399 Nabat, P., Carmichael, G. R., da Silva, A., Pistone, K., Chang, I., Gao, L., Wood, R., and Redemann, J.: Modeled
400 and observed properties related to the direct aerosol radiative effect of biomass burning aerosol over the Southeast
401 Atlantic, *Atmos. Chem. Phys.*, 22, 1-46, <https://doi.org/10.5194/acp-22-1-2022>, 2022.

402 Gordon, H., Field, P. R., Abe, S. J., Dalvi, M., Grosvenor, D. P., Hill, A. A., Johnson, B. T., Miltenberger, A. K.,
403 Yoshioka, M., and Carslaw, K. S.: Large simulated radiative effects of smoke in the south-east Atlantic, *Atmos.*
404 *Chem. Phys.*, 18, 15261-15289, doi:10.5194/acp-18-15261-2018, 2018.

405 Grund, C. J., and Eloranta, E. W.: University of Wisconsin high spectral resolution lidar, *Opt. Eng.*, 30, 6-12, 1991.

406 Gupta, S., McFarquhar, G. M., O'Brien, J. R., Poellot, M. R., Delene, D. J., Miller, R. M., and Small Griswold, J. D.:
407 Precipitation Susceptibility of Marine Stratocumulus with Variable Above and Below-Cloud Aerosol
408 Concentrations over the Southeast Atlantic, *Atmos. Chem. Phys. Discuss. [preprint]*, [https://doi.org/10.5194/acp-](https://doi.org/10.5194/acp-2021-677)
409 2021-677, in review, 2021.

410 Hair, J. W., Hostetler, C. A., Cook, A. L., Harper, D. B., Ferrare, R. A., Mack, T. L., Welch, W., Izquierdo, L. R.,
411 Hovis, F. E.: Airborne High Spectral Resolution Lidar for profiling aerosol optical properties, *Appl. Optics*, 47, doi:
412 10.1364/AO.47.006734, 2008.

Formatted: Font: 10 pt, Complex Script Font: 10 pt

Deleted: Discuss. [preprint],

Deleted: 2021-333, in review

Deleted: 1

Formatted: Font: 10 pt, Complex Script Font: 10 pt

Formatted: Indent: Before: 0", Hanging: 0.13"

Deleted: ¶

417 [Haywood, J. M., Abel, S. J., Barrett, P. A., Bellouin, N., Blyth, A., Bower, K. N., Brooks, M., Carslaw, K., Che, H.,](#)
418 [Coe, H., Cotterell, M. I., Crawford, I., Cui, Z., Davies, N., Dingley, B., Field, P., Formenti, P., Gordon, H., de](#)
419 [Graaf, M., Herbert, R., Johnson, B., Jones, A. C., Langridge, J. M., Malavelle, F., Partridge, D. G., Peers, F.,](#)
420 [Redemann, J., Stier, P., Szpek, K., Taylor, J. W., Watson-Parris, D., Wood, R., Wu, H., and Zuidema, P.: The](#)
421 [CLoud–Aerosol–Radiation Interaction and Forcing: Year 2017 \(CLARIFY-2017\) measurement campaign, *Atmos.*](#)
422 [Chem. Phys., 21, 1049–1084, <https://doi.org/10.5194/acp-21-1049-2021>, 2021.](#)
423 [Kacarab, M., Thornhill, K. L., Dobracki, A., Howell, S. G., O'Brien, J. R., Freitag, S., Poellot, M. R., Wood, R.,](#)
424 [Zuidema, P., Redemann, J., and Nenes, A.: Biomass burning aerosol as a modulator of the droplet number in the](#)
425 [southeast Atlantic region, *Atmos. Chem. Phys.*, 20, 3029–3040, <https://doi.org/10.5194/acp-20-3029-2020>, 2020.](#)
426 Keil, A., and Haywood, J. M.: Solar radiative forcing by biomass burning aerosol particles during SAFARI 2000: A
427 case study based on measured aerosol and cloud properties, *J. Geophys. Res. Atmos.*, 108, 8467,
428 doi:10.1029/2002JD002315, 2003.
429 Klopfer, D., Formenti, P., Namwoonde, A., Cazaunau, M., Chevaillier, S., Feron, A., Gaimoz, C., Hease, P., Lahmidi,
430 F., Mirande-Bret, C., Triquet, S., Zeng, Z., and Piketh, S. J.: Chemical composition and source apportionment of
431 atmospheric aerosols on the Namibian coast, *Atmos. Chem. Phys.*, 20, 15,811–15,833, doi:10.5194/acp-20-15811-
432 2020, 2020.
433 Koch, D., and Del Genio A. D.: Black carbon semi-direct effects on cloud cover: review and synthesis, *Atmos. Chem.*
434 *Phys.*, 10, 7685–7696, doi:10.5194/acp-10-7685-2010, 2010.
435 Lu, Z., Liu, X., Zhang, Z., Zhao, C., Meyer, K., Rajapakshe, C., Wu, C., Yang, Z., and Penner, J.: Biomass smoke
436 from southern Africa can significantly enhance the brightness of stratocumulus over the southeastern Atlantic
437 Ocean, *Proc. Natl. Acad. Sc.*, 115, 2924–2929, doi:10.1073/pnas.1713703115, 2018.
438 McFarquhar, G. M., and Wang, H.: Effects of aerosols on trade wind cumuli over the Indian Ocean: Model
439 simulations, *Q. J. R. Meteorol. Soc.*, 132, 821–843, doi: 10.1256/qj.04.179, 2006.
440 Mechoso, C. R., Wood, R., Weller, R., Bretherton, C. S., Clarke, A. D., Coe, H., Fairall, C., Farrar, J. T., Feingold,
441 G., Garreaud, R., Grados, C., McWilliams, J., de Szoeko, S. P., Yuter, S. E., and Zuidema, Z.: Ocean–cloud–
442 atmosphere–land interactions in the Southeastern Pacific: The VOCALS program, *B. Am. Meteorol. Soc.*, 95, 357–
443 375, doi:10.1175/BAMS-D-11-00246.1, 2013.
444 Meyer, K., Platnick, S., Oreopoulos, L., and Lee, D.: Estimating the direct radiative effect of absorbing aerosols
445 overlying marine boundary layer clouds in the southeast Atlantic using MODIS and CALIOP, *J. Geophys. Res.*
446 *Atmos.*, 118, 4801–4815, doi:10.1002/jgrd.50449, 2013.
447 Müller, D., Wandinger, U., and Ansmann, A.: Microphysical particle parameters from extinction and backscatter lidar
448 data by inversion with regularization: theory, *Appl. Optics*, 38, 2346–2357, 1999a.
449 Müller, D., Wandinger, U., and Ansmann, A.: Microphysical particle parameters from extinction and backscatter lidar
450 data by inversion with regularization: simulation, *Appl. Optics*, 38, 2358–2368, 1999b.
451 Müller, D., Hostetler, C. A., Ferrare, R. A., Burton, S. P., Chemyakin, E., Kolgotin, A., Hair, J. W., Cook, A. L.,
452 Harper, D. B., Rogers, R. R., Hare, R. W., Cleckner, C. S., Obland, M. D., Tomlinson, J., Berg, L. K., and Schmid,
453 B.: Airborne multiwavelength high spectral resolution lidar (HSRL-2) observations during TCAP 2012: vertical
454 profiles of optical and microphysical properties of a smoke/urban haze plume over the northeastern coast of the US,
455 *Atmos. Meas. Tech.*, 7, 3487–3496, doi:10.5194/amt-7-3487-2014, 2014.
456 Müller, D., Chemyakin, E., Kolgotin, A., Ferrare, R. A., Hostetler, C. A., and Romanov, A.: Automated, unsupervised,
457 inversion of multiwavelength lidar data with TiARA: assessment of retrieval performance of microphysical
458 parameters using simulated data, *Appl. Optics*, 58, 4981–5007, doi:10.1364/AO.58.004981, 2019.
459 Painemal, D., Kato, S., and Minnis, P.: Boundary layer regulation in the southeast Atlantic cloud microphysics during
460 the biomass burning season as seen by the A-train satellite constellation, *J. Geophys. Res. Atmospheres*, 119,
461 11,288–211,302, doi:10.1002/2014JD022182, 2014.
462 Penner, J. E., Zhang, S. Y., and Chuang, C. C.: Soot and smoke aerosol may not warm climate, *J. Geophys. Res.*
463 *Atmospheres*, 108, 4657, doi:10.1029/2003JD003409, 2003.
464 [Pistone, K., Zuidema, P., Wood, R., Diamind, M., da Silva, A. M., Ferrada, G., Saide, P. E., Ueyama, R., Ryoo, J.-](#)
465 [M., Pfister, L., Podolske, J., Noone, D., Bennett, R., Stith, E., Carmichael, G., Redemann, J., Flynn, C., LeBlanc,](#)
466 [S., Segal-Rozenhaimer, M., and Shinozuka, Y.: Exploring the elevated water vapor signal associated with the free](#)
467 [tropospheric biomass burning plume over the southeast Atlantic Ocean, *Atmos. Chem. Phys.*, 21, 9643–9668,](#)
468 <https://doi.org/10.5194/acp-21-9643-2021>, 2021.
469 Pósfai, M., Simonić, R., Li, J., Hobbs, P. V., and Buseck, P. R.: Individual aerosol particles from biomass burning in
470 southern Africa: 1. Compositions and size distributions of carbonaceous particles, *J. Geophys. Res.*, 108, 8483,
471 doi:10.1029/2002JD002291, 2003.

Formatted: Font: 10 pt, Complex Script Font: 10 pt

Formatted: Indent: Before: 0", Hanging: 0.13"

Formatted: Font: 10 pt, Complex Script Font: 10 pt

Formatted: Font: 10 pt, Complex Script Font: 10 pt

472 Ramanathan, V., Crutzen, P. J., Kiehl, J. T., and Rosenfeld, D.: Aerosols, climate, and the hydrological cycle, *Science*,
473 294(5549), 2119-2124, doi:10.1126/science.1064034, 2001.

474 Randles, C.A., daSilva, A. M., Buchard, V., Colarco, P. R., Darmenov, A., Govindaraju, P., Smirnov, A., Holben, B.,
475 Ferrare, R. A., Hair, J., Shinozuka, Y., and Flynn, C. J.: The MERRA-2 aerosol reanalysis, 1980 onward. Part I:
476 System description and data assimilation evaluation, *J. Climate*, 30, 6823–6850, doi: 10.1175/JCLI-D-16-0609.1,
477 2017.

478 Redemann, J., Wood, R., Zuidema, P., Doherty, S. J., Luna, B., LeBlanc, S. E., Diamond, M. S., Shinozuka, Y., Chang,
479 I. Y., Ueyama, R., Pfister, L., Ryoo, J.-M., Dobracki, A. N., da Silva, A. M., Longo, K. M., Kacenelenbogen, M.
480 S., Flynn, C. J., Pistone, K., Knox, N. M., Piketh, S. J., Haywood, J. M., Formenti, P., Mallet, M., Stier, P.,
481 Ackerman, A. S., Bauer, S. E., Fridlind, A. M., Carmichael, G. R., Saide, P. E., Ferrada, G. A., Howell, S. G.,
482 Freitag, S., Cairns, B., Holben, B. N., Knobelspiesse, K. D., Tanelli, S., L'Ecuyer, T. S., Dzambo, A. M., Sy, O. O.,
483 McFarquhar, G. M., Poellot, M. R., Gupta, S., O'Brien, J. R., Nenes, A., Kacarab, M., Wong, J. P. S., Small-
484 Griswold, J. D., Thornhill, K. L., Noone, D., Podolske, J. R., Schmidt, K. S., Pilewskie, P., Chen, H., Cochrane, S.
485 P., Sedlacek, A. J., Lang, T. J., Stith, E., Segal-Rozenhaimer, M., Ferrare, R. A., Burton, S. P., Hostetler, C. A.,
486 Diner, D. J., Seidel, F. C., Platnick, S. E., Myers, J. S., Meyer, K. G., Spangenberg, D. A., Maring, H., and Guo, L.:
487 An overview of the ORACLES (ObseRvations of Aerosols above Clouds and their intEractionS) project: aerosol-
488 cloud-radiation interactions in the southeast Atlantic basin, *Atmos. Chem. Phys.*, 21, 1507-1563, doi:10.5194/acp-
489 21-1507-2021, 2021.

490 Rogers, R. R., Hair, J. W., Hostetler, C. A., Ferrare, R. A., Obland, M. D., Cook, A. L., Harper, D. B., Burton, S. P.,
491 Shinozuka, Y., McNaughton, C. S., Clarke, A. D., Redemann, J., Russell, P. B., Livingston, J. M., and Kleinman,
492 L. I.: NASA LaRC airborne high spectral resolution lidar aerosol measurements during MILAGRO: observations
493 and validation, *Atmos. Chem. Phys.*, 9, 4811-4826, 2009.

494 Ryoo, J.-M., Pfister, L., Ueyama, R., Zuidema, P., Wood, R., Chang, I., and Redemann, J.: A meteorological
495 overview of the ORACLES (ObseRvations of Aerosols above CLOUDs and their intEractionS) campaign over the
496 southeastern Atlantic during 2016–2018: Part I – Climatology, *Atmos. Chem. Phys.*, 21, 16689–16707,
497 <https://doi.org/10.5194/acp-21-16689-2021>, 2021.

498 Sakaeda, N., Wood, R., and Rasch, P. J.: Direct and semidirect aerosol effects of southern African biomass burning
499 aerosol, *J. Geophys. Res. Atmospheres*, 116, D12205, doi:10.1029/2010JD015540, 2011.

500 Sawamura, P., Moore, R. H., Burton, S. P., Chemyakin, E., Müller, D., Kolgotin, A., Ferrare, R. A., Hostetler, C. A.,
501 Ziemba, L. D., Beyersdorf, A. J., and Anderson, B. E.: HSRL-2 aerosol optical measurements and microphysical
502 retrievals vs. airborne in situ measurements during DISCOVER-AQ 2013: an intercomparison study, *Atmos. Chem.*
503 *Phys.*, 17, 7229-7243, doi.org/10.5194/acp-17-7229-2017, 2017.

504 Schmid, B., Ferrare, R. A., Flynn, C., Elleman, R., Covert, D., Strawa, A., Welton, E., Turner, D., Jonsson, H.,
505 Redemann, J., Eilers, J., Ricci, K., Hallar, A. G., Clayton, M., Michalsky, J., Smirnov, A., Holben, B., and Barnard,
506 J. : How well do state-of-the-art techniques measuring the vertical profile of tropospheric aerosol extinction
507 compare? *J. Geophys. Res.*, 111, D05S07, doi:10.1029/2005JD005837, 2006.

508 She, C. Y., Alvarez II, R. J., Caldwell, L. M., and Krueger, D. A.: High-spectral-resolution Rayleigh-Mie lidar
509 measurement of aerosol and atmospheric profiles, *Opt. Lett.*, 17, 541-543, 1992.

510 Shinozuka, Y., Saide, P. E., Ferrada, G. A., Burton, S. P., Ferrare, R. A., Doherty, S. J., Gordon, H., Longo, K., Mallet,
511 M., Feng, Y., Wang, Q., Cheng, Y., Dobracki, A., Freitag, S., Howell, S. G., LeBlanc, S., Flynn, C., Segal-
512 Rozenhaimer, M., Pistone, K., Podolske, J. R., Stith, E. J., Bennett, J. R., Carmichael, G. R., da Silva, A.,
513 Govindaraju, R., Leung, R., Zhang, Y., Pfister, L., Ryoo, J.-M., Redemann, J., Wood, R., and Zuidema, P.: Modeling
514 of the smoky troposphere of the southeast Atlantic: a comparison to ORACLES airborne observations from
515 September of 2016, *Atmos. Chem. Phys.*, 20, 11491-11526, doi:10.5194/acp-20-11491-2020, 2020.

516 Shipley, S. T., Tracy, D. H., Eloranta, E. W., Tauger, J. T., Stroga, J. T., Roesler, F. L., and Weinman, J. A.: High
517 spectral resolution lidar to measure optical scattering properties of atmospheric aerosols. 1. Theory and
518 instrumentation, *Appl. Optics*, 22, 3716-3724, 1983.

519 Stein, A.F., Draxler, R. R., Rolph, G. D., Stunder, B. J. B., Cohen, M. D., and Ngan, F.: NOAA's HYSPLIT
520 atmospheric transport and dispersion modeling system, *B. Am. Meteorol. Soc.*, 96, 2059-2077, doi:10.1175/BAMS-
521 D-14-00110.1, 2015.

522 Veselovskii, I., Kolgotin, A., Grazianov, V., Müller, D., Wandinger, U., and Whiteman, D. N.: Inversion with
523 regularization for the retrieval of tropospheric aerosol parameters from multi-wavelength lidar sounding, *Appl.*
524 *Optics*, 41, 3685-3699, 2002.

525 Wilcox, E. M.: Stratocumulus cloud thickening beneath layers of absorbing smoke aerosol, *Atmos. Chem. Phys.*, 10,
526 11769-11777, doi:10.5194/acp-10-11769-2010, 2010.

Formatted: Font: 10 pt, Complex Script Font: 10 pt

Formatted: Indent: Before: 0", Hanging: 0.13"

Deleted: ¶

528 Wilcox, E. M.: Direct and semi-direct radiative forcing of smoke aerosols over clouds, *Atmos. Chem. Phys.*, 12, 139-
529 149, doi:10.5194/acp-12-139-2012, 2012.
530 Yamaguchi T, Feingold, G., Kazil, J., and McComiskey, A.: Stratocumulus to cumulus transition in the presence of
531 elevated smoke layers. *Geophys. Res. Lett.*, 42: 10478–10485, 2015.
532 Zhang Z., Meyer, K., Yu, H., Platnick, S., Colarco, P. R., Liu, Z., and Oreopoulos, L.: Shortwave direct radiative
533 effects of above-cloud aerosols over global oceans derived from 8 years of CALIPSO and MODIS observations,
534 *Atmos. Chem. Phys.*, 16, 2877-2900, doi:10.5194/acp-16-2877-2016, 2016.
535 Zhang, X., Mao, M., Yin, Y., and Tang, S.: The absorption Ångström exponent of black carbon with brown coatings:
536 effects of aerosol microphysics and parameterization, *Atmos. Chem. Phys.*, 20, 9701-9711, doi:10.5194/acp-20-
537 9701-2020, 2020.
538 Zuidema, P., Redemann, J., Haywood, J., Wood, R., Piketh, S., Hipondoka, M., and Formenti, P.: Smoke and clouds
539 above the southeast Atlantic, *B. Am. Meteorol. Soc.*, 97, 1131-1135, doi:10.1175/BAMS-D-15-00082.1, 2016.
540 Zuidema, P., Sedlacek III, A. J. Flynn, C., Springston, S., Delgado, R., Zhang, J., Aiken, A. C., Koontz, A., and
541 Muradyan, P.: The Ascension Island boundary layer in the remote Southeast Atlantic is often smoky, *Geophys. Res.*
542 *Lett.*, 45, 4456-4465, doi:10.1002/2017/GL076926, 2018.
543

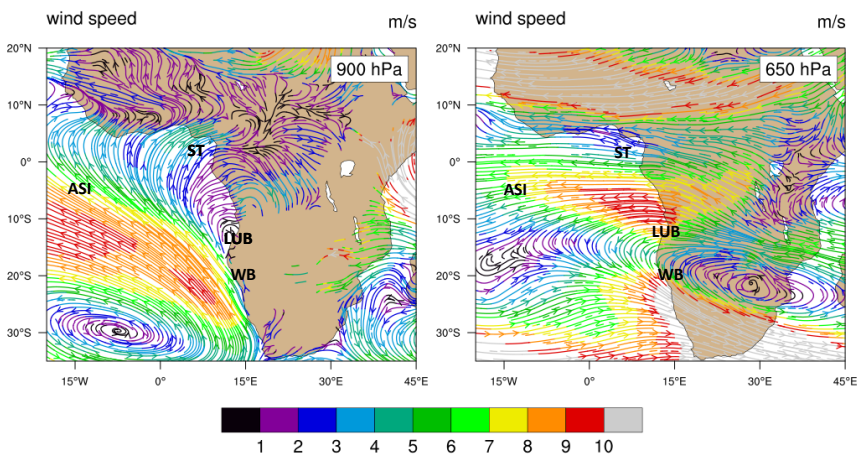
544
545
546

Table 1: Averaging area, flight time periods, the duration over water and number of HYSPLIT backward trajectories, and number of HSRL-2 profiles in each grid box used in the study.

| Box | Averaging Area | Averaging Days | Time of Day | Duration in Hours Over Water at 3.5 km | Number of Profiles |
|-----|--------------------------|----------------|-------------|--|--------------------|
| A | 11° S-9° S; 1° W-1° E | 9/12,16 | 11:00 UTC | 44.3±7.0 (N = 19) | 50 |
| B | 10° S-8° S; 8° E-10° E | 9/12,16,18 | 10:00 UTC | 14.9±4.5 (N = 27) | 56 |
| C | 16° S-14° S; 4° E-6° E | 9/12,16 | 13:00 UTC | 40.4±7.2 (N = 19) | 51 |
| D | 14° S-12° S; 10° E-12° E | 9/18,24 | 09:00 UTC | 5.5±2.0 (N = 27) | 46 |
| E | 23° S-21° S; 8° E-10° E | 9/20,22 | 14:00 UTC | - | 36 |

547

Deleted: ¶
-----Page Break-----
¶



552
 553
 554
 555
 556
 557

Figure 1: MERRA2 monthly mean reanalysis of 900 and 650 hPa streamlines for September 2016. Stations marked are Ascension Island (ASI), Lubango (LUB), a long-term AERONET site at 2 km elevation, and Walvis Bay (WB), where ER-2 flights originated from during the September 2016 ORACLES IOP. Flights in August 2017 and September/October 2018 originated from São Tomé (ST).

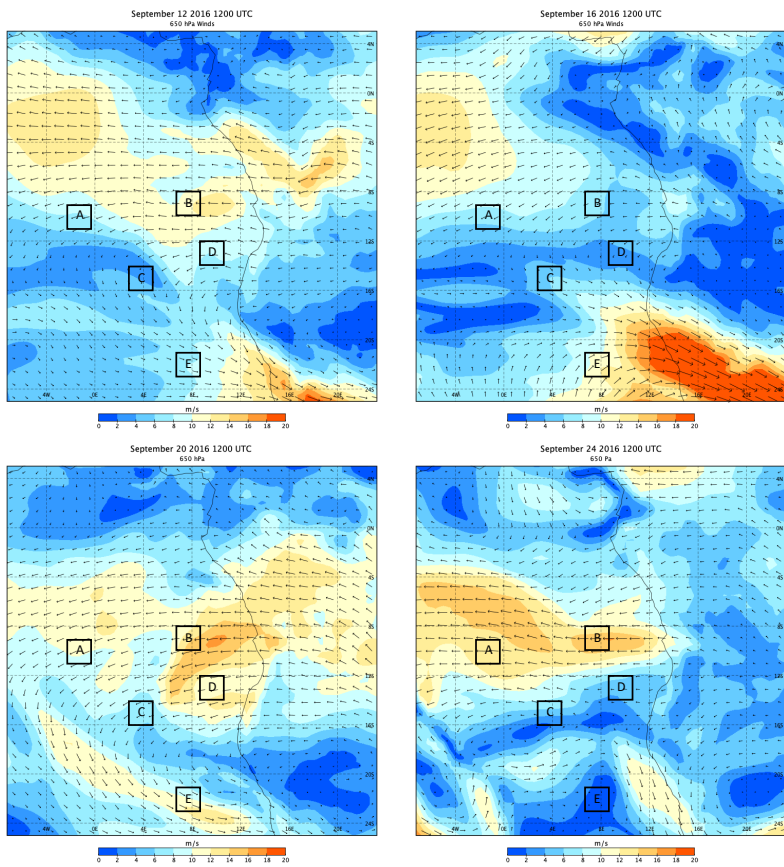
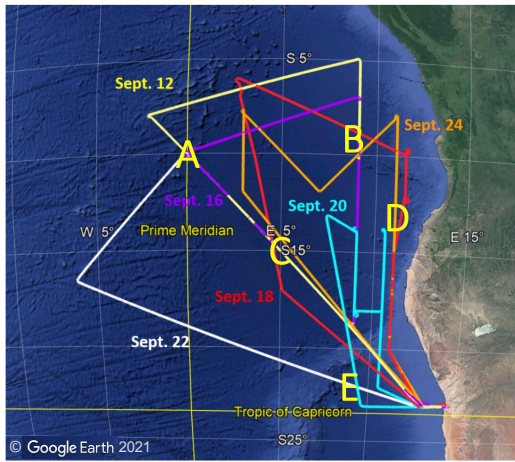


Figure 2: MERRA2 reanalysis of 650 hPa winds at 1200 UTC on September 12, 16, 20, 24, 2016. Grid boxes in the study are marked with letters.

558
559
560
561

562
563



564
565
566
567
568

Figure 3: HSRL-2 science data flight tracks during the September 2016 IOP. Letters refer to the grid boxes identified in Fig. 2

Formatted: Indent: Before: 1.38", First line: 0"
Deleted: 2

570

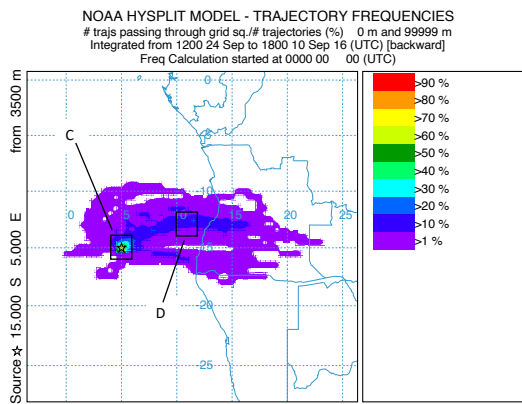
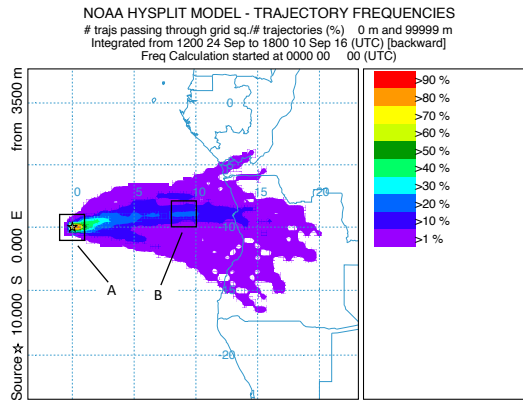


Figure 4: Frequency distribution of 48-hour backward trajectories of air parcels arriving at 3500 m above the centers of grid boxes A and C over the time period of the campaign. Grid boxes B and D are upstream of grid boxes A and C, respectively.

571
572
573
574
575
576

Deleted: 3

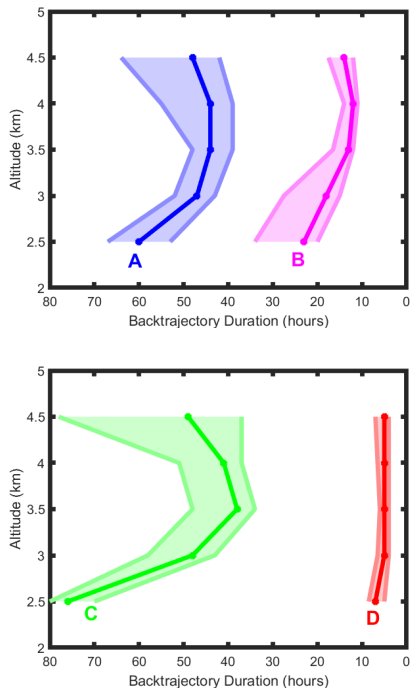


Figure 5: Duration of time spent over water of air parcels arriving at grid boxes marked on the figure. Solid lines are median values and the shaded portion are the range of the 75th and 25th percentile. The number of trajectories used for the calculation are in Table 1. Trajectory hours are shown in reverse to correspond to the map in Fig. 4.

579
580
581
582
583
584
585

Deleted: 4

Deleted: 3

Deleted: 1

589

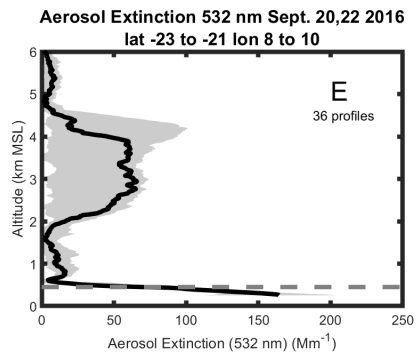
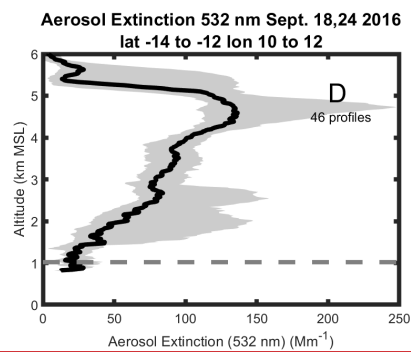
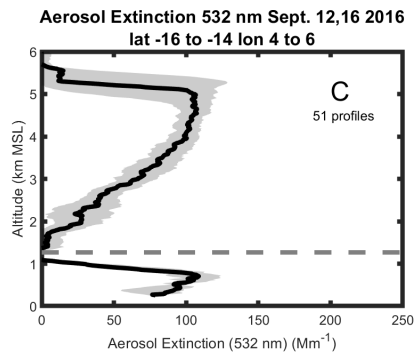
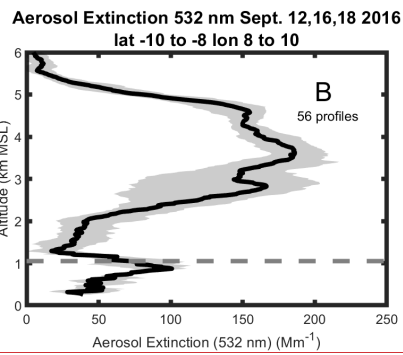
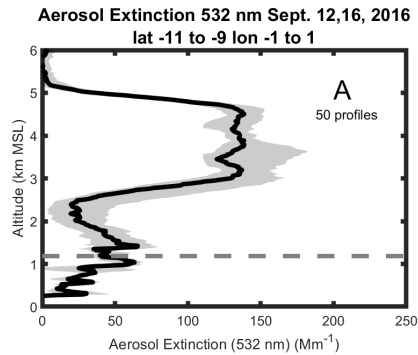


Figure 6: Average vertical profiles of the aerosol extinction coefficient at 532 nm in grid boxes A (upper left), B (upper right), C (middle left), D (middle right) and E (lower left). The averaging area, dates of flights and total number of one-minute profiles are also shown. The dark line represents the median value and grey shades contain the 25th to 75th percentiles. Dashed line refers to the mean cloud top height.

590

591

592

593

594

595

596

597

598

Deleted: 1

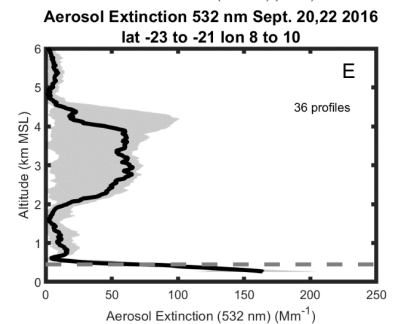
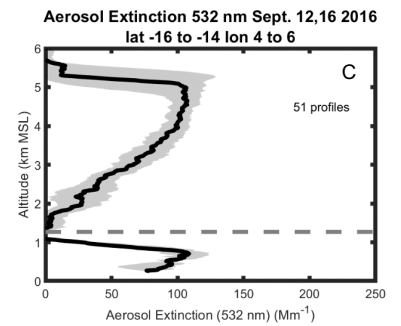
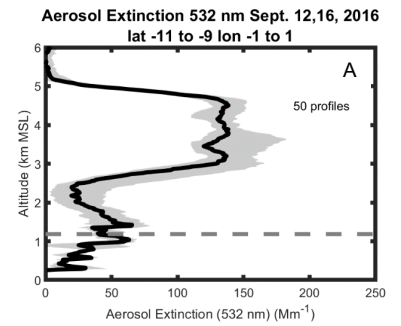
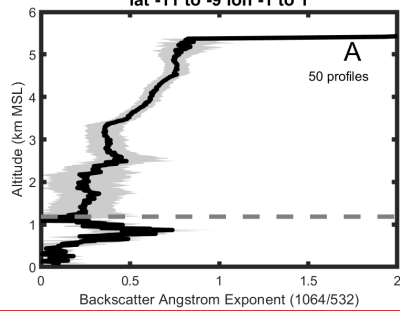


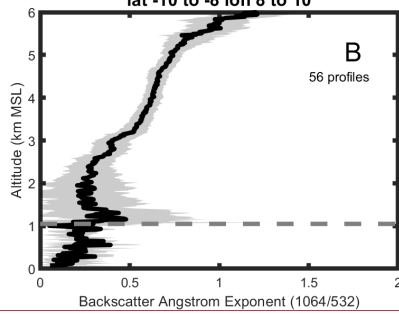
Figure 5: Average vertical profiles of the aerosol extinction coefficient at 532 nm in grid boxes A (upper left), B (upper right), C (middle left), D (middle right) and E (lower left). The averaging area, dates of flights and total number of one-minute profiles are also shown. The dark line represents the median value and grey shades contain the 25th to 75th percentiles. Dashed line refers to the mean cloud top height.

608

Backscatter Ang. Expo. 1064/532 Sept. 12,16, 2016
lat -11 to -9 lon -1 to 1

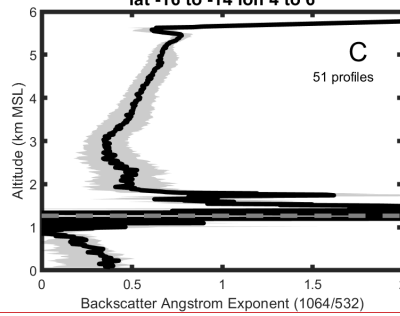


Backscatter Ang. Expo. 1064/532 Sept. 12,16,18 2016
lat -10 to -8 lon 8 to 10

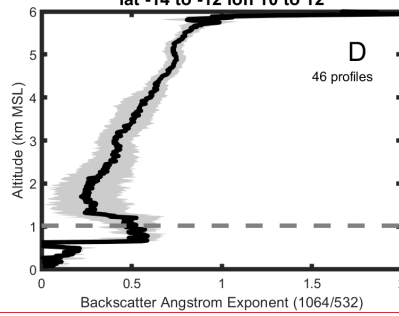


609

Backscatter Ang. Expo. 1064/532 Sept. 12,16 2016
lat -16 to -14 lon 4 to 6

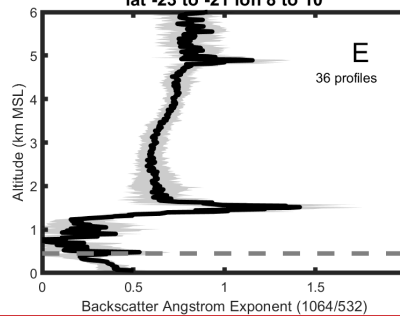


Backscatter Ang. Expo. 1064/532 Sept. 18,24 2016
lat -14 to -12 lon 10 to 12



610

Backscatter Ang. Expo. 1064/532 Sept. 20,22 2016
lat -23 to -21 lon 8 to 10



611

612

613

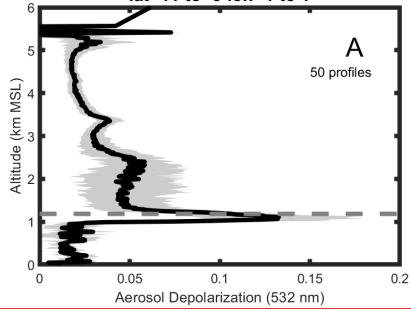
614

615

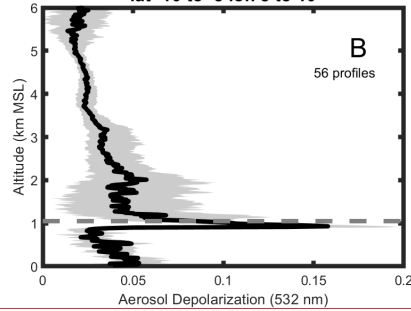
Figure 7: As in Fig. 6 but for the Wavelength Dependent Backscatter Ångström exponent between 1064 and 532 nm.

616

**Aerosol Depolarization 532 nm Sept. 12,16, 2016
lat -11 to -9 lon -1 to 1**

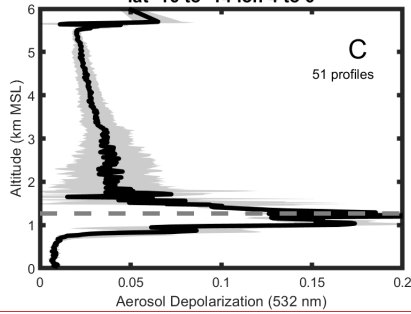


**Aerosol Depolarization 532 nm Sept. 12,16,18 2016
lat -10 to -8 lon 8 to 10**

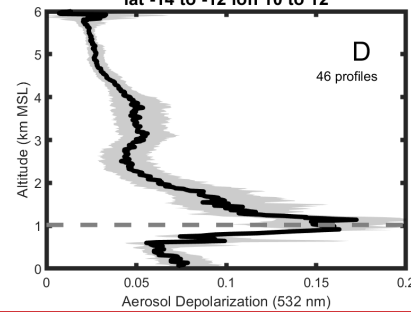


617

**Aerosol Depolarization 532 nm Sept. 12,16 2016
lat -16 to -14 lon 4 to 6**

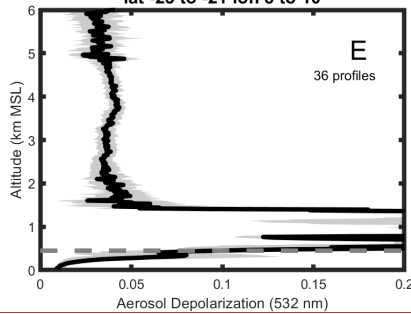


**Aerosol Depolarization 532 nm Sept. 18,24 2016
lat -14 to -12 lon 10 to 12**



618

**Aerosol Depolarization 532 nm Sept. 20,22 2016
lat -23 to -21 lon 8 to 10**



619

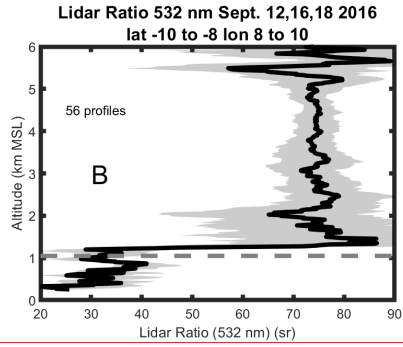
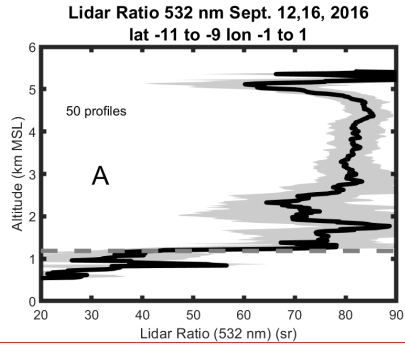
620

621

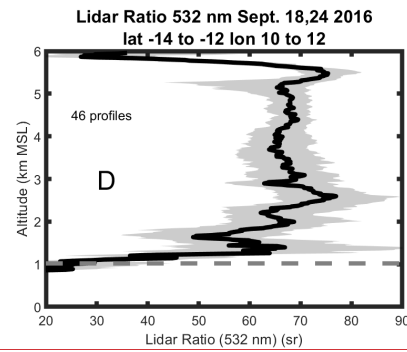
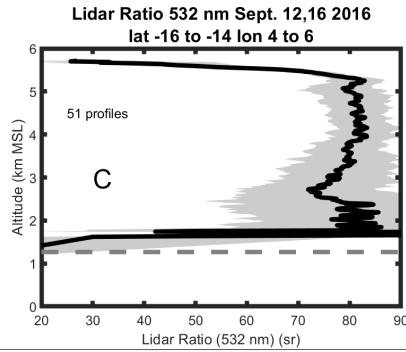
622

Figure 8: As in Fig. 6 but for the aerosol depolarization at 532 nm.

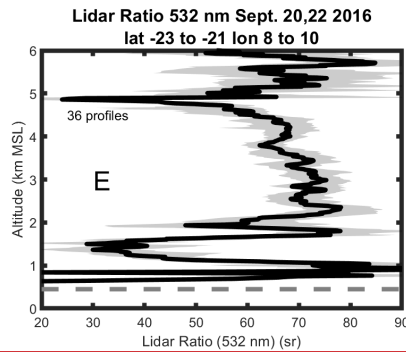
623



624



625



626

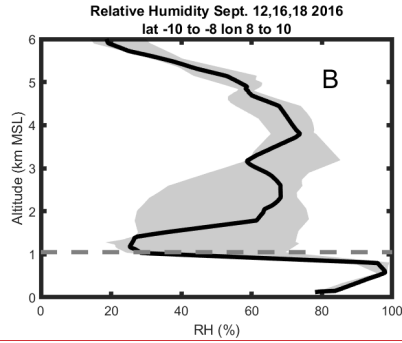
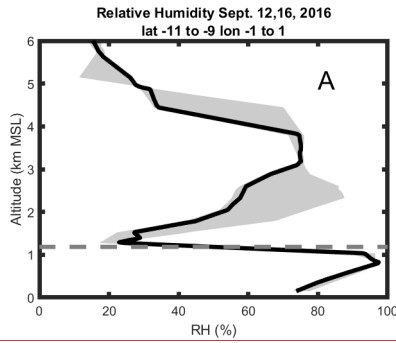
627

628

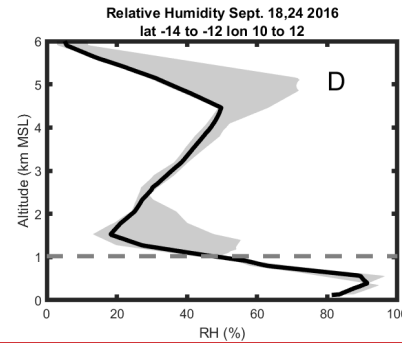
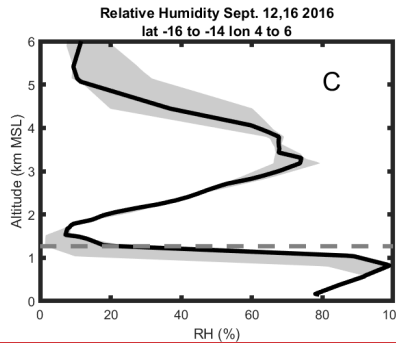
629

Figure 9: As in Fig. 6 but for the Lidar Ratio at 532 nm.

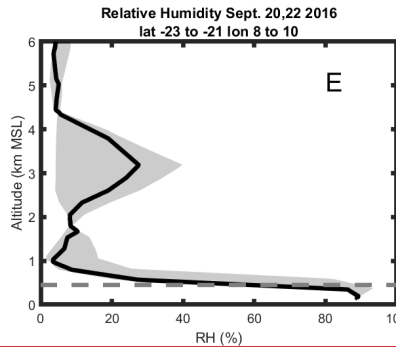
630



631



632



633

634

635

636

637

638

639

Figure 10: Relative Humidity (%) in grid boxes A (upper left), B (upper right), C (middle left), D (middle right) and E (lower left) from MERRA2 reanalysis corresponding to the HSRL-2 profiles shown in Figs. 6-9. The dark line represents the median value and grey shades contain the 25th to 75th percentiles. Dashed line refers to the mean cloud top height.

Formatted: Centered

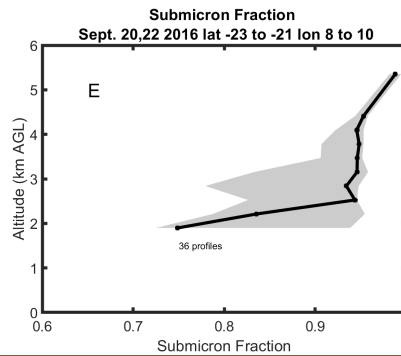
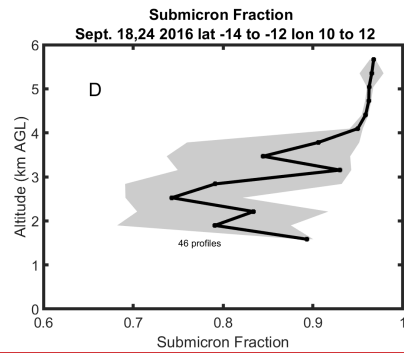
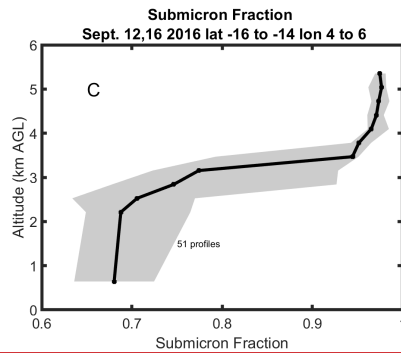
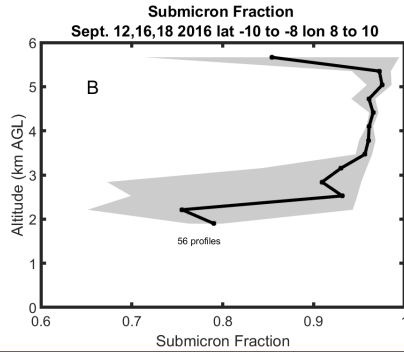
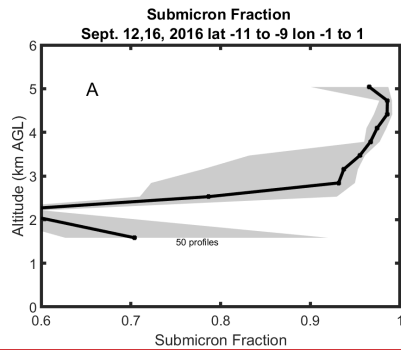
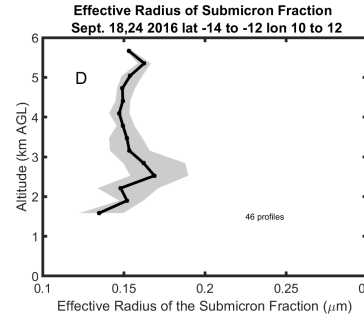
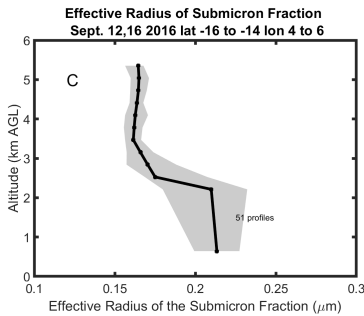
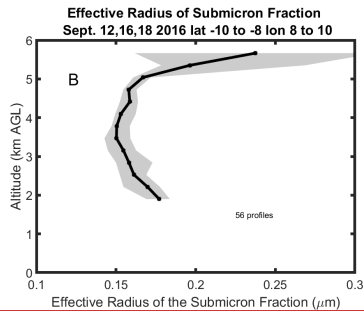
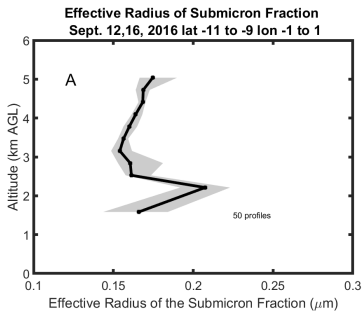


Figure 11: Average vertical profiles of the submicron fraction in grid boxes A (upper left), B (upper right), C (middle left), D (middle right) and E (lower left). The averaging area, dates of flights and total number of one-minute profiles in the average are also shown. The dark line represents the median value and grey shades contain the 25th to 75th percentiles.

649



650

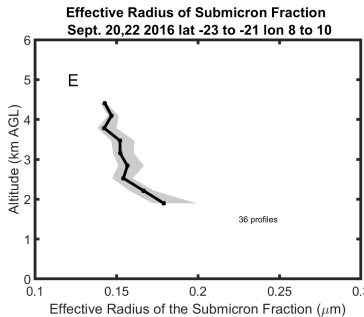


Figure 12: As in Fig. 11 but for the effective radius of the submicron fraction.

651

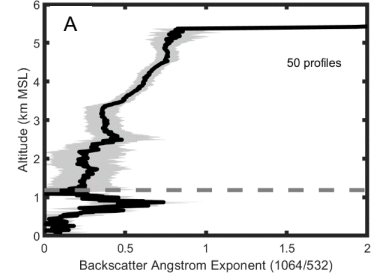
652

653

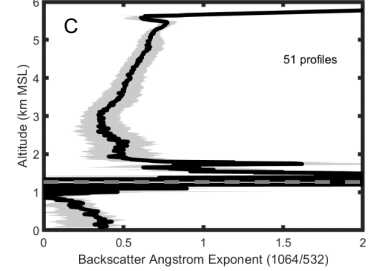
654

Deleted:

Backscatter Ang. Expo. 1064/532 Sept. 12,16, 2016 lat -11 to -9 lon -1 to 1



Backscatter Ang. Expo. 1064/532 Sept. 12,16 2016 lat -16 to -14 lon 4 to 6



Backscatter Ang. Expo. 1064/532 Sept. 20,22 2016 lat -23 to -21 lon 8 to 10

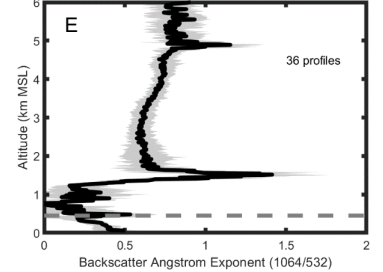


Figure 6: As in Fig. 5 but for the Wavelength Dependent Backscatter Angström exponent between 1064 and 532 nm.

Page Break

